

Impact of the Stable Solid-Electrolyte Interphase in Sustainable and High-Performance Lithium-Ion Battery Anodes

Merin Pulikkottil, Rakhi Raghavan Baby, and Seema Ansari*

Lithium-ion batteries (LIBs) have drawn significant attention in the electric vehicle industry, and activated carbon-based anodes are widely recognized as a cost-effective alternative to conventional anode materials. However, the application of these anode materials is significantly limited by the formation of an unstable solid-electrolyte interface (SEI). This study introduces nutmeg shell waste-derived activated carbon (ACNM) as a viable anode material for LIBs with a particular focus on the role of SEI in determining their electrochemical behavior and battery performance. The hierarchical pore structure in ACNM is achieved through systematic optimization of synthesis parameters, ensuring a balance

between surface area and the stability of the SEI. The combination of micropores and mesopores in ACNM effectively minimizes extensive SEI formation and associated capacity loss. The potential of ACNM for LIB anode applications is validated by fabricating anode half cells that exhibit a maximum specific capacity of 610 mAh g^{-1} . The half cells also show good cycling performance with significant rate capability. Using scanning electrochemical microscopy, the local electrochemical activity and formation of the SEI layer are investigated. This study highlights the suitability of ACNM for anode applications in LIBs and the importance of SEI engineering for next-generation LIBs.

1. Introduction

There is an ever-growing demand for lithium-ion batteries (LIBs) as they are accelerating the transition towards a greener future of transportation. However, conventional anode materials are creating challenges in this endeavor due to their limitations, such as high costs, limited resources, and environmental concerns. To address these issues, researchers are exploring alternative anode materials that are more sustainable, cost-effective, and remarkably efficient to meet future energy demands.^[1,2] Activated carbon (AC) is a widely recognized sustainable alternative that is highly relevant in this context. Its high surface area and tunable porosity provide numerous sites for lithium-ion intercalation, contributing to its capacity.^[3] The specific structural characteristics and performance of AC anodes can vary based on the choice of precursors and activation process used for their preparation. The production and utilization of biomass-derived AC (BDAC)

is an eco-friendly initiative that reduces bio-waste, ensuring resource efficiency and promoting a circular economy. In addition, BDAC helps in reducing the carbon footprint associated with traditional carbon production methods. Moreover, biomass waste is often abundant and readily available, making it a cost-effective option for AC production that reduces reliance on fossil fuels and minimizes environmental impact. BDAC-based anodes also have advantages including excellent cycle stability, better safety, high lithium storage capacity, improved lithium intercalation, excellent coulombic efficiency, high mechanical stability, and good rate capability.^[4–6]

In the state of the art, a diverse range of BDAC such as rice husk, coconut shells, corn cobs, and woody biomass have been used as anode material for energy storage applications.^[7–11] In a recent study by Hernández-Rentero and his coworkers, BDAC was investigated for its application in LIBs.^[12] The study demonstrated significant improvements in electrochemical performance and lithium storage capabilities for LIBs. Additionally, Z.Liu and his group explored the use of BDAC as anode materials in LIBs showing promising performance in terms of reversible capacity.^[10] The work by M.Khan et al. highlighted the tunability of porous carbonaceous materials derived from renewable resources, showcasing their potential for energy storage applications.^[5] These studies collectively underscore the promising prospects of BDAC as sustainable and high-performance electrode materials in LIB systems.

Nevertheless, the formation of the solid electrolyte interface (SEI) on the surface of the anode material constitutes a pivotal element in the working of LIBs. The decomposition of the electrolyte during the initial charging and discharging cycles leads to the creation of SEI, which is a thin, passivating layer that forms on the anode surface through the electrochemical reduction of

M. Pulikkottil, S. Ansari
Centre for Materials for Electronics Technology (C-MET)
Research Centre
University of Calicut
Thrissur 680581, India
E-mail: seema@cmet.gov.in

R. Raghavan Baby
Centre for Sustainable Energy Technologies
CSIR
National Institute of Interdisciplinary Science and Technology (CSIR-NIIST)
Thiruvananthapuram, Kerala 695019, India

R. Raghavan Baby
Academy of Scientific and Innovative Research (AcSIR)
Ghaziabad 201002, India

 Supporting information for this article is available on the WWW under <https://doi.org/10.1002/batt.202500228>

electrolytes in the LIB. The SEI prevents further breakdown of the electrolyte and stabilizes the interface between the anode and the electrolyte. It acts as a barrier between the highly reactive anode material and electrolyte while facilitating the movement of lithium ions through it. SEI also ensures long-term cycling stability, minimum active material loss, better safety, and enhanced performance of LIBs.^[13–15] As discussed earlier, the irreversible capacity loss during initial charging and discharging cycles contributes to a drop in coulombic efficiency. However, the formation of a stable SEI minimizes further lithium and electrolyte losses, thereby improving the overall efficiency of batteries. Furthermore, SEI plays a crucial role in ensuring the safety of LIB by preventing thermal runaway and controlling the formation of lithium dendrites. In contrast, the unstable formation of SEI causes continuous decomposition of electrolytes, leading to irreversible capacity loss and poor performance of the LIBs. Additionally, a thick or resistive SEI layer may hinder lithium-ion transport within these systems. Poorly formed SEI can lead to battery failure associated with rapid capacity loss and enhanced internal resistance. So understanding the SEI is essential for improving the efficiency and stability of anode material in LIBs.^[5,16]

The structural properties of anode materials have a crucial role in the formation and stability of SEI. The anode materials with high surface areas often lead to thicker and nonuniform SEI layers owing to the availability of more active sites for electrolyte decomposition. In comparison with crystalline materials, amorphous materials are more likely to develop an unstable SEI as they promote localized SEI formation. Additionally, the mechanical properties of anode materials are essential to prevent unnecessary volume expansion during lithiation and delithiation processes.^[17] The chemical reactivity of the anode material can further result in the formation of less stable SEI layers. The materials with high electronic conductivity even facilitate electron distribution and SEI formation, while those with high ionic conductivity promote efficient lithium-ion transport through the SEI. Interfacial properties like wettability and adhesion between the anode and the electrolyte are also important in determining the uniformity and stability of the SEI layer.^[18] However, a large surface area and high porosity in AC can lead to the formation of a thicker SEI during initial charging-discharging cycles. This issue can be addressed by optimizing the porous distribution and surface area of the AC-based anode material. A controlled porous structure in AC-based anodes can prevent excessive formation of SEI, reduce initial capacity loss, and enhance the cycle life of LIBs.^[12]

In this work, the nutmeg shell waste was used as the precursor for the preparation of BDAC due to its inherent lignocellulosic nature. The shells contain lignin (50–59%), cellulose (11–28%), and hemicellulose (9–16%) of their total dry weight. This specific composition is advantageous for producing BDAC with a well-developed pore distribution.^[19–21] Thus, this nutmeg-derived AC (ACNM) has better structural properties which is beneficial for electrode applications in LIBs.^[5,6,15] Additionally, the use of ACNM offers a sustainable and environmentally friendly approach to utilizing nutmeg waste material and a cost-effective alternative to commercially available AC, which is often derived from non-renewable sources.^[6] In the following sections, we shall discuss the development of porous ACNMs and insights into their

remarkable material and electrochemical properties. Further, the emphasis is given to optimize the activation ratio and to carbonize temperature for preparing ACNM.

The suitability of ACNM for LIB applications was validated by fabricating anode half-cells. The study provides valuable insights into SEI formation and its impact on the overall performance of the LIB system. A significant specific capacity value of 610 mAh g⁻¹ is exhibited by the fabricated half-cell at a current rate of 0.1 C. Additionally, we examined the cycle stability and rate capability of the as-fabricated half-cells. Recently, scanning electrochemical microscopy (SECM) has emerged as a versatile tool for studying the formation and stability of SEI. SECM is a scanning probe technique that provides insights into localized electrochemical processes at interfaces.^[22,23] The interface studies with SECM highlight the formation of the SEI layer on the anode surface and its subsequent impact on battery performance. To the best of our knowledge, little to no work has been reported on the aforementioned studies. Overall, this work demonstrates the suitability of ACNM as a practical and affordable anode material for fabricating LIBs.

2. Results and Discussion

2.1. Material Characterization of ACNMs

The pristine nutmeg shells (NMS) were subjected to thermogravimetry (TGA-DTA) analysis to explore the thermal degradation behavior. TGA-DTA curves are shown in Figure 1a representing three distinct portions of mass loss stages indicating the presence of hemicelluloses, lignin, and cellulose in NMS.^[6,24] Around the temperature of 120 °C, highly volatile compounds undergo breakdown along with water evaporation and cause initial weight loss. The thermal decomposition of hemicellulose occurs in the temperature range of 120–250 °C. For a temperature above 250 °C, cellulose undergoes decomposition. The major mass loss occurs between 360 and 550 °C representing lignin degradation.^[25,26]

Figure 1b displays the Raman spectra of developed ACNMs that provide essential insights into the structural characteristics of as-prepared AC. All spectra are identical and display characteristic wide peaks. The peak around 1355 cm⁻¹ represents the D band corresponding to the disordered sites in the sample, whereas, the E_{2g} symmetric phonon vibrations can be identified from the G band around 1580 cm⁻¹. Raman spectra of ACNMs represent the availability of graphite and disordered carbon structure in them.^[27,28] The values of intensity ratio (I_D/I_G) for ACNM-1-700, ACNM-2-700, and ACNM-3-700 were 0.94, 1.05, and 1.11, respectively. The increase in values of I_D/I_G ratio indicates that the activation ratio is responsible for defects in the graphitic structure. ACNM-2-500, ACNM-2-600, ACNM-2-700, and ACNM-2-800 have I_D/I_G values of 0.87, 0.98, 1.05, and 1.01, respectively that represent the incomplete graphitization at lower temperatures and distorted graphitic structure at higher carbonization temperatures.^[29,30] This structure is related to the limited atomic mobility of carbon atoms at lower temperatures and the rapid movement of carbon atoms at higher temperatures.

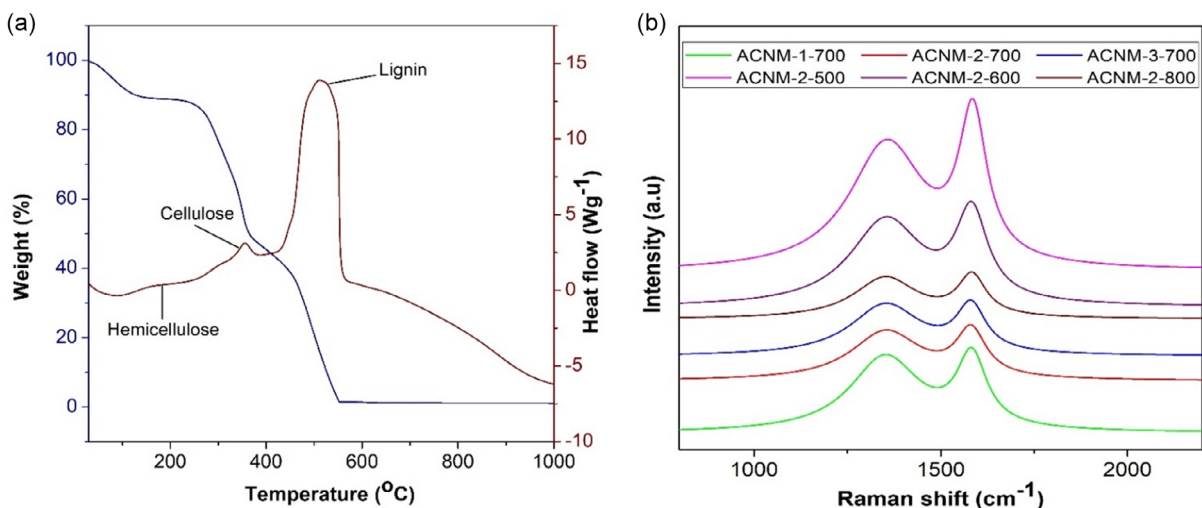


Figure 1. a) TGA curve of pristine nutmeg shell waste and b) Raman spectra of ACNMs.

Ultimately, this structure leads to a higher concentration of disordered sites.^[5]

The presence of defects and disordered sites in AC significantly influences the performance of LIB systems, with the I_D/I_G ratio serving as a key quantitative indicator. A higher I_D/I_G ratio represents a higher level of disorder that may lead to capacity fading during cycling and reduced rate capability. In contrast, a lower I_D/I_G ratio is related to an ordered structure which may limit the storage capacity. Therefore, a moderate value of I_D/I_G ratio can offer additional lithium storage along with sufficient capacity and a stable cycle life.^[31] Additionally, the I_D/I_G ratio has a significant impact on SEI formation. The higher value of the I_D/I_G ratio is typically associated with the chances of forming a thick and unstable SEI layer. ACNM-3-700 and ACNM-2-800 exhibit large I_D/I_G ratios, indicating thicker SEI layer formation and irreversible loss in capacity when used as anodes in LIBs.^[32,33] These results suggest the potential of ACNM-2-700 as an anode material with an optimum I_D/I_G ratio value.

Figure 2a shows X-ray diffraction (XRD) spectra of ACNMs. All the samples exhibit identical XRD patterns, indicating the presence of a graphitic nature alongside remarkable surface cavities. The spectra contain two broad peaks around $2\theta = 24^\circ$ and 43° . These characteristic peaks represent (002) and (100) planes of carbon as referenced in the ICDD database (ICDD PDF No: 01-075-1621).^[11,34] These planes indicate interlayer condensation and a significant regularity in crystalline structure, respectively. These features contribute positively to the formation of a stable SEI. However, the broadness of these peaks is related to the amorphous nature of the as-prepared AC, which provides a large surface area and active sites for electrolyte decomposition. This may lead to the formation of a heterogeneous SEI layer. Since ACNM-2-700 has the lowest FWHM value, it is more likely to develop a stable SEI layer compared to the other ACNM-X-Ys.^[35,36]

The pore distribution in anode materials determine the energy storage efficiency for battery applications. The nitrogen adsorption-desorption isotherms were studied to identify the

porous structure present in ACNMs which is displayed in Figure 2b. All the materials show type I isotherm indicating the microporous nature of the electrode materials. In the lower relative pressure region, the volume adsorbed rises sharply and remains unchanged in the higher relative pressure region. The development of micropores in ACNMs may be due to intercalation and deintercalation of potassium. The H4-type hysteresis loop present in the isotherms can be related to the availability of mesopores in their structure.^[37,38]

Figure 2c, d represent the distribution of the pores in ACNMs. The surface areas and pore volume of ACNMs were tabulated in Table 1. These data confirm that lignin content in precursor material significantly contributes to the micropores in ACNMs. The surface area of ACNM-X-Y increases as the activation ratio rises from 1 to 3. The carbonization temperature also has a superior role in determining the porosity of these materials. The surface area of the as-prepared AC rises with carbonization temperature up to 700 °C and beyond this temperature, the surface area is reduced.^[39,40] The carbonization temperature aids in the surface area till the temperature reaches 700 °C.

As carbonization temperature further increases, it causes a reduction in the surface area of as-prepared AC.^[40,41] This indicates the development of porous structure followed by structural collapse at higher temperatures. The obtained results indicate that ACNM-3-700 has the largest surface area, with a major contribution from the microporous structure. However, the availability of both micropores and mesopores in ACNM-2-700 facilitates the accessible surface area that in turn improves electrochemical charge storage.^[42]

The surface area analysis of anode material is a highly reliable tool for predicting the feasibility of SEI formation in LIBs. The micropores available in the anode material can lead to excessive SEI formation and electrolyte decomposition. Meanwhile, the presence of mesopores creates a more stable and uniform SEI.^[17,43] Even though the large surface area and pore volume are beneficial for lithium-ion intercalation, they can also lead to extensive SEI layer formation and capacity loss.^[13] On comparing the as-prepared anode materials, ACNM-2-700 shows the

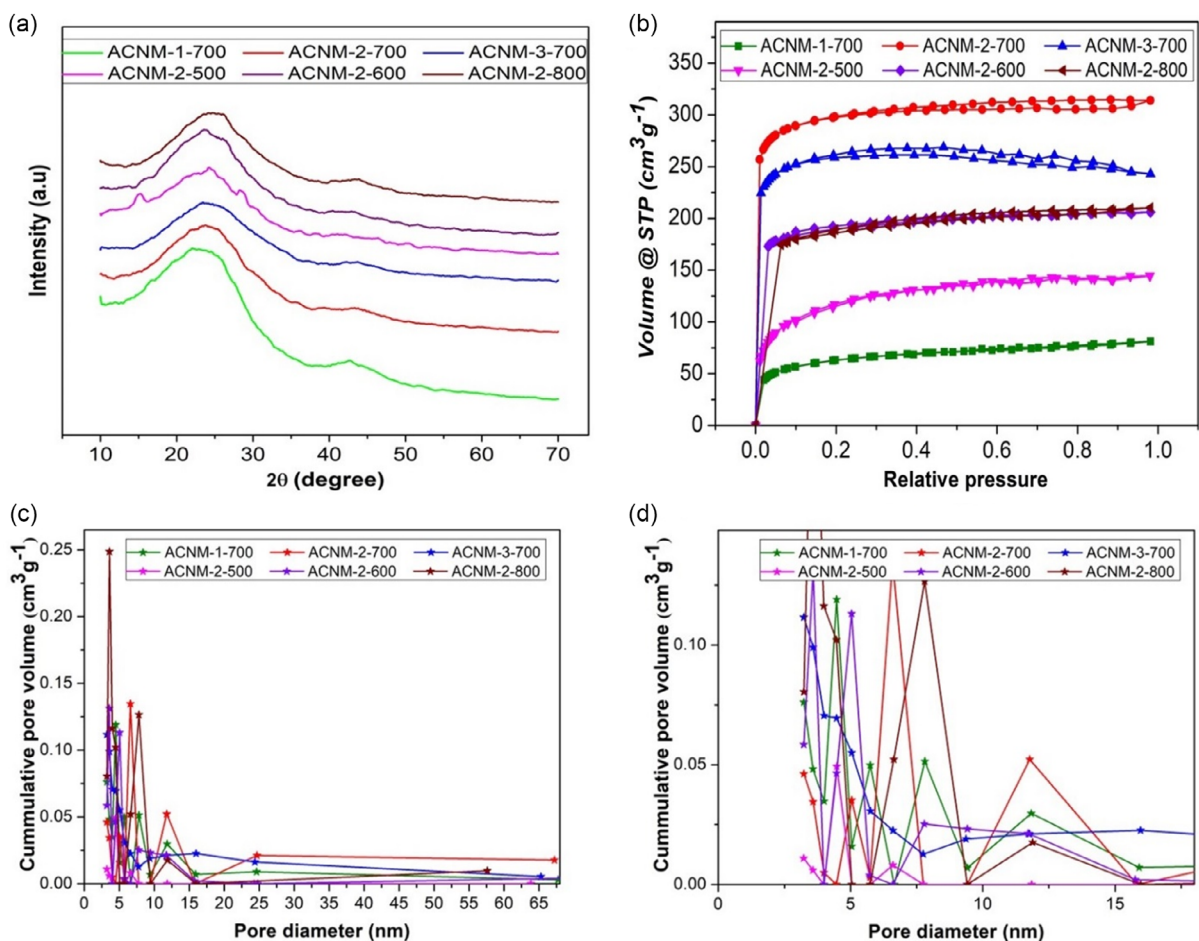


Figure 2. a) XRD spectra, b) N_2 adsorption–desorption isotherms, c) pore distribution curves, and d) enlarged pore distribution curves of ACNMs.

Table 1. Structural parameters and elemental analysis of ACNMs.

Sample name	Surface area [$m^2 g^{-1}$]			Pore volume [$cm^3 g^{-1}$]			Diameter [nm]		Elemental analysis [wt%]	
	Micro pores	Meso pores	Total	Micro pores	Meso pores	Total	C	O		
ACNM-1-700	170	20	230	0.073	0.028	0.126	2.18	88.3	11.73	
ACNM-2-700	851	50	1011	0.239	0.770	0.960	3.24	91.7	8.3	
ACNM-3-700	1092	9	1177	0.426	0.023	0.486	1.65	92.3	7.7	
ACNM-2-500	123	3	256	0.101	0.004	0.160	2.50	82.5	17.5	
ACNM-2-600	691	19	764	0.262	0.026	0.318	1.66	90.2	9.8	
ACNM-2-800	342	35	432	0.173	0.047	0.224	2.06	91.3	8.7	

highest contribution of mesopores which benefits lithium storage efficiency due to its high surface area and helps minimize excessive SEI formation.^[16] This observation is also consistent with that from Raman spectroscopy and XRD analysis of ACNMs.

The surface morphology of ACNMs was identified using SEM analysis. The presence of an interconnected porous structure was evident from the SEM images shown in Figure 3. This type of well-distributed porous structure improves the assessable surface area, enabling rapid electrolyte diffusion. Consequently, this increases the electrochemical efficiency of

the electrode material.^[44,45] The SEM images demonstrate the significant effect of activation ratio and carbonization temperature on the pore structure development in the synthesis of ACNM. In addition, the porous distribution became more defined with the rise in carbonization temperature.^[27,46] However, on further increase in temperature above 700 °C causes a high degree of porosity along with thin structural walls.^[24] Energy dispersive spectroscopy (EDS) was performed for elemental analysis of ACNMs and the results are presented in Table 1. All the ACNMs show a high carbon ratio over oxygen.

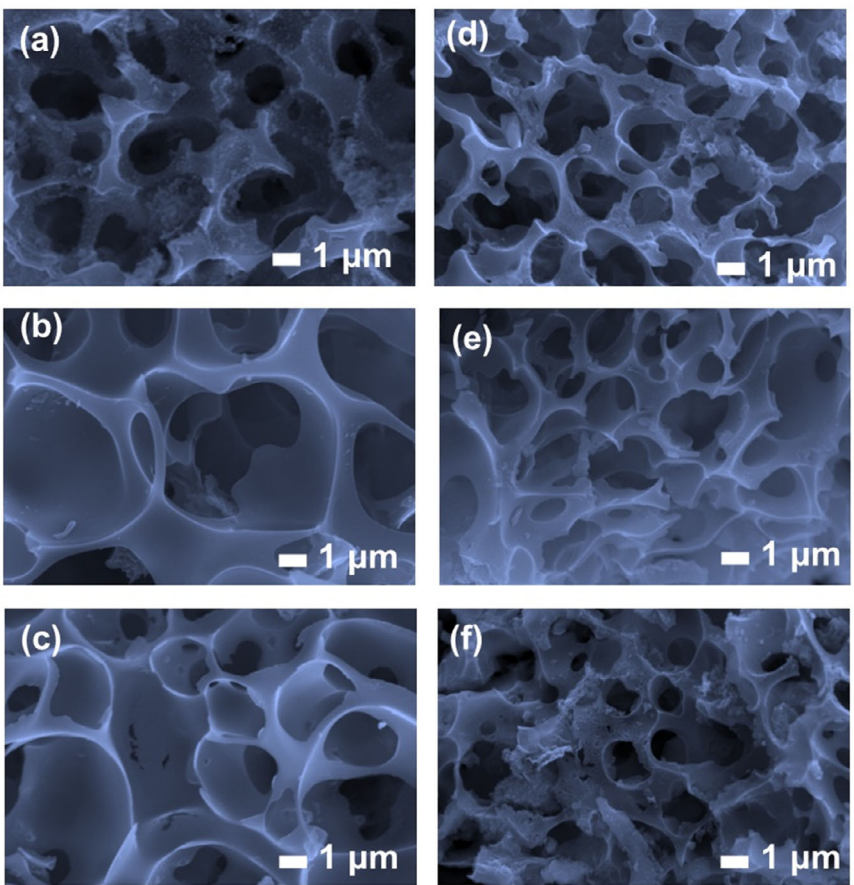


Figure 3. SEM images of a) ACNM-1-700, b) ACNM-2-700, c) ACNM-3-700, d) ACNM-2-500, e) ACNM-2-600, and f) ACNM-2-800 at 20 000 \times magnification.

The structural micrographs obtained from HR-TEM are displayed in **Figure 4a**, representing the disordered porous structure available in the material. The availability of micro and meso pores over the surface of the anode material is beneficial for extensive charge storage capacity.^[47] Additionally, an adequate distribution of mesopore is visible from the TEM images facilitating better electrolyte wetting and ion transport. This is also favorable in the formation of a stable and uniform SEI in the anode material. The TEM images are consistent with the surface area analysis and suggest the feasibility of ACNM for anode applications in LIBs.^[48]

The X-ray photoelectron spectrometry (XPS) survey spectrum (**Figure 5b**) identifies the elements such as oxygen and carbon. **Figure 4c,d** show the C 1s and O 1s spectra of ACNM, respectively. The C 1s spectrum displays three characteristic peaks at \approx 284.6, 285.68, and 288.8 eV. These peaks correspond to the C–C bond, the C–O bond, and the O=C–O bond, respectively. The highest intensity of the C–C bond suggests that most of the carbon atoms in ACNM are arranged in a conjugated honeycomb structure.^[47] **Figure 4d** shows the O 1s spectra, which display two deconvoluted peaks at 530.2 and 531.33 eV. These peaks indicate the presence of various oxygen-containing functional groups and oxygen vacancies, respectively. The aromatic structure present in the lignin may be responsible for these oxygen-containing functional groups. The availability of these groups can lead to more reactive sites for electrolyte decomposition and result in a thicker or less stable

SEI layer. However, these groups can also enhance the surface wettability of the anode material and adhesion of the electrolyte which is advantageous for improving ion transport and SEI uniformity.^[48] These results are also consistent with the observations made in the Raman spectra.

All these material characterizations demonstrate the critical role of pore structure in SEI formation and suggest the potential of ACNM-2-700 as a highly promising candidate for anode applications in LIBs. The presence of mesopores in ACNM-2-700 ensures superior electrolyte infiltration, enabling stable and uniform SEI formation. Furthermore, its highly interconnected pore network promotes even electrolyte distribution, facilitating homogeneous SEI growth. The optimized surface area and abundant active sites further enhance SEI stability, contributing to exceptional long-term cycling performance. The subsequent sections validate these advantages by comparing the electrochemical performance of ACNM-2-700 with other anode materials in LIBs.

2.2. Study of the Suitability of ACNMs as LIB Anode Material

Anode half-cells were fabricated with lithium metal and ACNMs as cathode and anode material, respectively. The fabricated half-cells were then subjected to various electrochemical analyses to understand the lithium storage properties of ACNMs in LIBs. Cyclic voltammetry (CV) measurements at a scan rate of

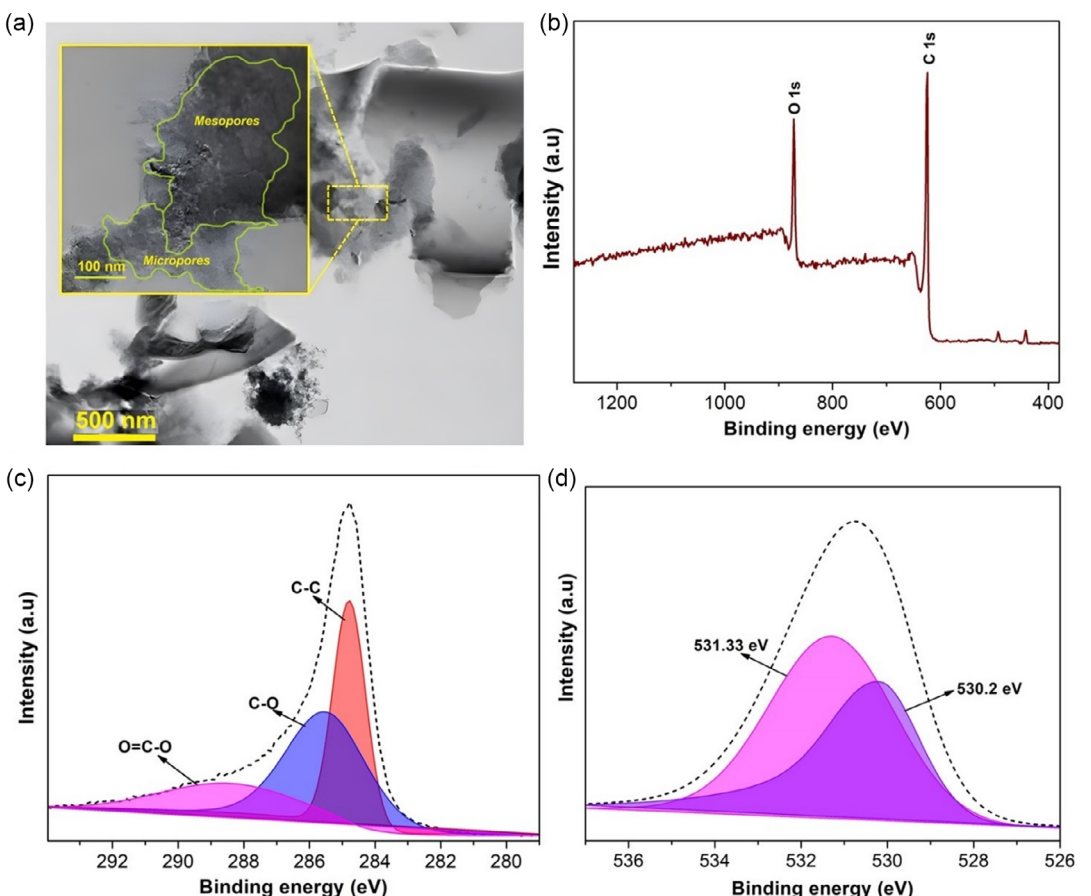


Figure 4. a) TEM micrographs of ACNM, b) XPS survey spectrum, c) C 1s spectrum, and d) O 1s spectrum of ACNM.

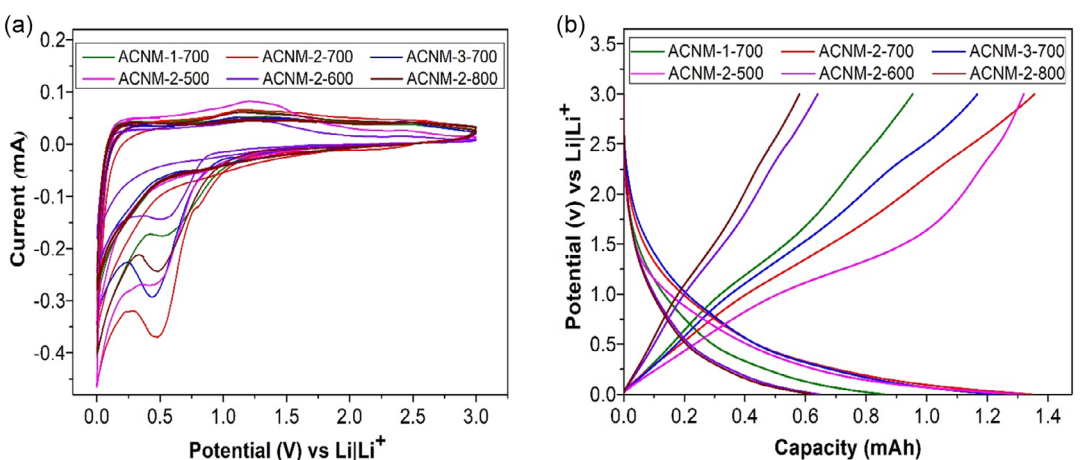


Figure 5. a) Cyclic voltammogram of anode half cell at a scan rate of 0.1 mV s^{-1} . b) The charge–discharge profile of the half cell at a current rate of 0.1 C.

0.1 mV s^{-1} , for a potential window of 0–3 V versus $\text{Li}^+|\text{Li}$ were carried out to evaluate the capacity of the fabricated anode half-cells. Galvanostatic cycling tests were also performed for the same voltage range at different C rates. The suitability of ACNM electrodes in LIBs was subsequently studied by combining the results of CV and Galvanostatic charge–discharge (GCD) measurements. EIS is carried out from 10 mHz to 100 kHz, with a voltage of 10 mV.

Figure 5a represents the cyclic voltammograms of ACNM-based anode half-cells at a scan rate of 0.1 mV s^{-1} in the potential window of 0–3 V versus $\text{Li}^+|\text{Li}$. The CV scan is repeated for five cycles, which resembles that of traditional amorphous carbon materials.^[49] The curves are irreversible and the first cycle shows a significant difference from the subsequent cycles, which is a typical characteristic of the carbon-based anodes in LIBs.^[50] The first cycle shows a broad peak extending below 1.0 V versus

$\text{Li}^+|\text{Li}$ and a small signal at about 0.7 V followed by a tilted line extending to 0.01 V versus $\text{Li}^+|\text{Li}$. This irreversible nature of the first cycle can be assigned to the partial electrolyte decomposition and SEI layer formation at the electrode/electrolyte interface.^[49,51] The irreversible reduction peaks observed in the first cycle of CV measurement demonstrate the formation of SEI and the loss of lithium ions associated with it.^[52]

The subsequent cycles are reversible and have a progressively overlapping profile with peaks around 0.01 V versus $\text{Li}^+|\text{Li}$, as the SEI has already formed. Additionally, the diminishing peaks in these subsequent cycles indicate the intercalation and deintercalation of the lithium ions into the disordered carbon along with lithium plating/stripping into the pores present in the active materials without further SEI formation.^[17,32] A slight shift and broadening of redox peaks may be ascribed to the increased resistance at the SEI layer. These overlapping cycles further indicate the irreversible decomposition of electrolytes and the presence of a well-formed SEI in the half-cell.^[53] The absence of any additional irreversible processes in subsequent CV curves also validates the stability of the SEI formed. This stability trend further demonstrates that the anode material's high surface area and well-defined porous structure make it ideal for LIB, as it offers sufficient sites for Li-ions to be inserted.^[54,55]

The specific capacity of the anode cells is calculated using the equations given below.

$$Q (\text{mAh g}^{-1}) = \int_{V_2}^{V_1} i(V) dV / (2 \times 3.6 \times m \times v) \quad (1)$$

where Q is the specific capacity (mAh g^{-1}), $\int_{V_2}^{V_1} i(V) dV$ is the total charge storage, m and v represent the mass of active material and scan rate, respectively. The capacity of a system is directly related

to the area under the CV curve. When the CV curve area decreases after the first cycle, it can lead to significant capacity loss. This initial capacity loss further validates the formation of SEI. After the first cycle, the CV curves overlap, indicating a stable system with perfect reversible capacity, even though there is a considerable irreversible capacity loss in the first cycle.^[54,56] The value of specific capacity calculated from CV is tabulated in Table 2.

ACNM-2-700-based half-cell is further investigated galvanostatically at different current rates. The GCD cycling was carried out over the voltage range of 0–3.0 V versus $\text{Li}^+|\text{Li}$. The charge-discharge profile of fabricated half-cells, at a current rate of 0.1 C are displayed in Figure 5b. ACNM-2-700 shows highest capacity which was found to be 610 mAh g^{-1} at a C rate of 0.1 C.

The values of specific capacity of all samples from GCD analyses were consolidated in Table 2. The presence of SEI significantly influences the GCD characteristics of an anode half-cell. The lithium loss occurred during the formation of SEI, is evident from the higher discharge capacity in the first GCD cycle than that in subsequent cycles. The state of the art specific capacity values of previously reported biomass-derived AC materials are compared with the present ACNM-2-700 and represented in the Table 3. These values confirm the remarkable capacity of the ACNM-based LIB system.

Further stability tests show that the anode half-cell shows excellent rate capability and cycling stability. The relationship between the capacity values of the fabricated half-cell and the current rate is displayed in Figure 6a. The capacity value exhibits a consistent decreasing trend with an increase in the current rate.

The rate capability test of the half-cell is carried out at different current rates for ten cycles each. Figure 6b represents the capacity at current rates of 0.1, 1, 2, 3, 4, 5, and 0.1 C. The reversible capacities are 610 , 307 , 211 , 186 , 169 , and 557 mAh g^{-1} , respectively. The capacity retention is found to be 91% after the rate capability test. The decrease in cell capacity at higher current rates is likely due to restricted lithium-ion diffusion through SEI, as the increased resistance from the SEI typically results in a significant capacity drop. However, the remarkable capacity retention observed here suggests efficient ion transport, indicating the presence of a well-formed SEI.^[57]

A stable SEI facilitates regular charging and discharging without electrolyte decomposition, which in turn improves the cycle stability of LIBs and ensures better capacity retention and slower capacity loss during cycling. Figure 7a represents a cycle test of

Table 2. Values of specific capacity of ACNMs.

Sample name	Capacity [mAh]		Specific capacity [mAh g ⁻¹]	
	From CV	From GCD	From CV	From GCD
ACNM-1-700	0.80	0.92	333	383
ACNM-2-700	1.32	1.52	574	610
ACNM-3-700	0.96	1.31	291	397
ACNM-2-500	1.17	1.44	344	422
ACNM-2-600	0.52	0.67	326	416
ACNM-2-800	0.48	0.65	302	404

Table 3. Specific capacity values of sustainable AC anode materials.

Precursor material	Activating agent	Specific capacity [mAh g ⁻¹]	Current rate [C]	Cycle test	References
Jute fiber	ZnCl ₂	534	0.2	79% @ C/5 current rate after 100 cycles	[1]
Pine cone	KOH	370	0.1	83% @ C/3 current rate after 100 cycles	[17]
Cherry pits	KOH	320	0.1	84% @ C/3 current rate after 200 cycles	[53]
Rice husk	NaOH	477	0.2	68% @ C/5 current rate after 100 cycles	[65]
Coffee waste	Air	359	0.2	72% @ C/5 current rate after 100 cycles	[66]
Pistachio shell	KOH	317	0.1	85% @ 2C current rate after 500 cycles	[67]
Nutmeg shell	KOH	610	0.1	84% @ 1C current rate after 200 cycles	Present work

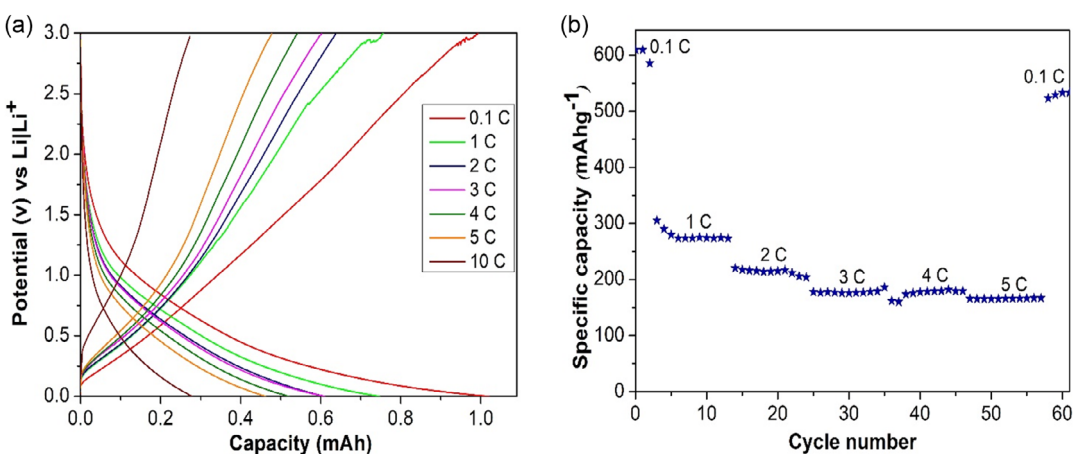


Figure 6. a) GCD profile of the half cell at various current rates. b) Variation in capacity during the rate capability test.

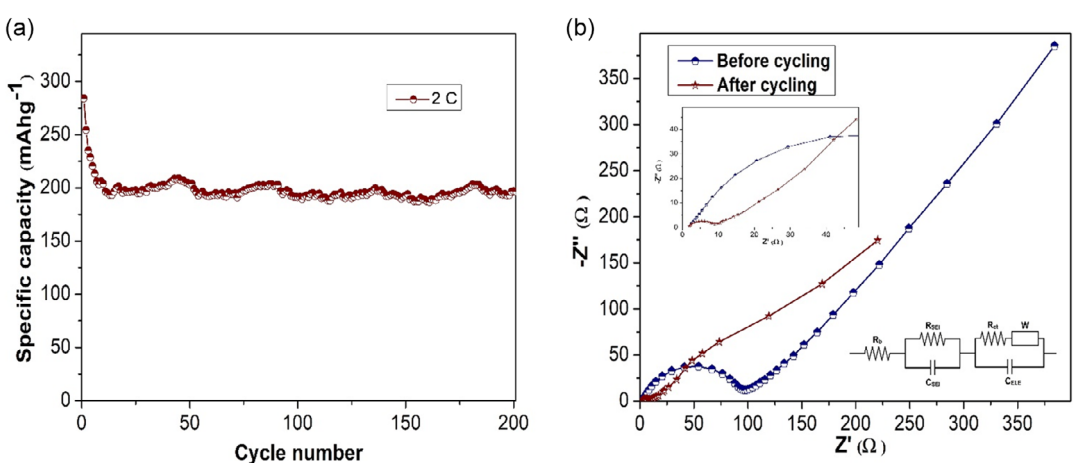


Figure 7. a) Cycling performance of anode half cell at a current rate of 2 C for 200 cycles. b) Nyquist plot of ACNM-2-700-based anode half cells before and after cycling with higher frequency region and equivalent circuit as inset.

the system at a current rate of 2 C for 200 cycles. The cycling performance is also very impressive, as the capacity value of 200 mAh g^{-1} is maintained even after 200 cycles. However, the value of specific capacity gradually decreases until the 33rd cycle. This may be due to the irreversible surface reactions and the hierarchical porous nature of the material.^[58]

The volume of the material expands as lithium ions are embedded during the cycling process and slightly subsides when the ions are released. Compared to bulk material, the structural collapse of hierarchical porous material occurs more frequently. In subsequent cycles, the material stabilizes and maintains discharge capacity. This can also be attributed to the formation of a more stable SEI layer at the interface between the anode and the electrolyte.^[59]

The Nyquist plot (Figure 7b) is used to study the formation of SEI and other electrochemical behavior of fabricated LIBs. The higher frequency region of the Nyquist plot reflects electrolyte resistance in the fabricated system. The deeply convoluted semicircle in the middle-to-high frequency reflects resistance associated with charge transfer resistance and the SEI layer present in the electrode/electrolyte interface of the LIB half-cell. Warburg

element represented by a tilted line with a slope around 45° in the low frequency indicates the semi-infinite diffusion.^[16] The curve contains a semicircle with a small diameter indicating lower SEI resistance and suggesting a well-formed SEI. This stable SEI enhances the performance of LIB. The curves can be related to an equivalent circuit consisting of elements such as R_b , R_{SEI} , C_{SEI} , R_{ct} , C_{ELC} , and W , where R_b represents the bulk resistance. The resistance due to charge transfer is given by R_{ct} . The resistance and capacitance of SEI is given by R_{SEI} and C_{SEI} . The values of C_{ELC} and W are related to the double-layer capacitance and lithium-ion diffusion on anode material, respectively.

Table 4 contains the values of these components before and after cycling experiments. The lower R_b and R_{ct} values demonstrate the formation of a stable SEI. Moreover, the reduction in ohmic and activation polarization during lithiation/delithiation processes is evident from these values. The effect of cycling is also clear from these Nyquist plots. A slight increase in R_b value suggests the aging of LIB over prolonged cycling. The smaller diameter of the semicircle after cycling may be ascribed to the decrease in charge transfer resistance. In the Nyquist plots, the Warburg element of the anode half-cell after cycling decreases,

Table 4. Components in equivalent circuits of anode half cell.

	R_b [Ω]	C_{SEI} [μF]	R_{SEI} [Ω]	R_{ct} [Ω]	C_{ELE} [μF]	W [$\Omega S^{-1/2}$]
Before cycling	2.12 ± 0.11	3.84 ± 0.23	79.50 ± 0.23	5.03 ± 0.23	2.14 ± 2.94	79.98 ± 1.84
After cycling	2.42 ± 0.25	1.05 ± 0.12	108.60 ± 0.12	5.77 ± 0.12	21.1 ± 0.43	18.30 ± 1.78

confirming the presence of a thin SEI.^[60,61] These observations are consistent with those of CV and GCD.

2.3. Mapping of SEI Layer on the Surface of Anode with SECM

SECM is used to study the formation of SEI on ACNM-based anode electrodes. SECM analysis was performed on pristine and cycled (after the first cycle and after 200 cycles) anode electrodes with an ultramicroelectrode of diameter $\approx 15 \mu m$ in a three-electrode configuration. $Fe(CN)_6^{3-}/Fe(CN)_6^{4-}$ is employed as a redox mediator

for the analysis. **Figure 8a** represents the schematic illustration of the SECM experimental setup.

Here, the SECM area scan is used to investigate the surface of anodes and understand the changes associated with the formation of SEI. The information related to the surface is obtained from the tip current, which is a function of the tip position. The approach method was employed to identify the closest distance for receiving current feedback, and the z-position was fixed before starting the area scan in the x–y direction. The current profile obtained reflects the surface of the anode under study and is associated with the electrochemical behavior of the

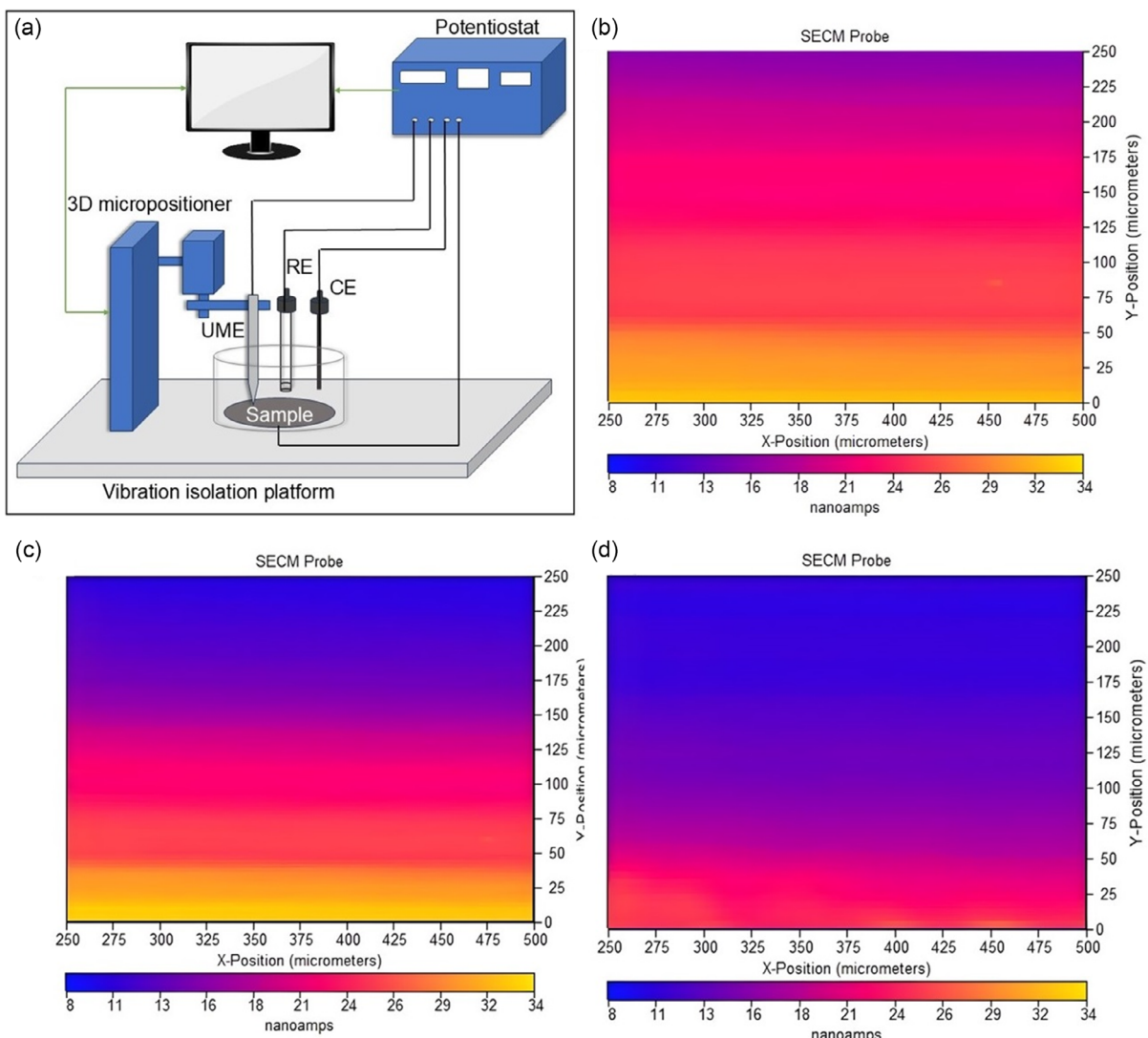


Figure 8. a) Schematic illustration of SECM experimental setup. SECM area scan measurement of b) pristine anode, c) after the first cycle, and d) after 200 cycles of charging and discharging.

surfaces. This data is represented as a color pattern, with each color corresponding to the respective current value.^[22,62]

The SECM was recorded in positive feedback mode in an area scan of 250 μm × 250 μm. Figure 8b–d illustrates the area scan of anode material, that is pristine, after the first cycle and after 200 cycles, respectively. These figures reveal a randomly distributed SEI layer, which may be attributed to the high surface area and porosity of the anode material.^[63] In the pristine anode (Figure 8b), the current profile is relatively uniform, with minor variations corresponding to the local topography. However, after cycling, SEI is randomly distributed across the electrode surface.^[12] Figure 8c displays the heterogeneous evolution of the interface on the anode after the first cycle. The SECM image obtained for cycled anode material (Figure 8d) indicates the presence of insulating SEI regions that are unevenly distributed across the surface.^[62] Significant reductions in the current profile after cycling further confirmed the formation of a well-defined SEI. The SECM analysis is also consistent with the electrochemical behavior of the obtained CV curves. The irreversible capacity loss associated with the first cycle charging and discharging is also validated from the observations of the SECM analysis.^[64] Overall, ACNM has demonstrated remarkable performance in terms of specific capacity, cyclability, availability of well-formed SEI, and rate capability, making it a promising anode material for LIBs.

3. Conclusion

In conclusion, we have developed AC with an enhanced surface area and hierarchical porous structure from nutmeg shell waste through chemical activation using KOH, followed by carbonization. By fine-tuning the activation ratio and carbonization temperature, a total of six samples were prepared, in which sample ACNM-2-700 ended up with a large surface area of 1011 m² g⁻¹ and pore volume of 0.960 cm³ g⁻¹. The Raman analysis of the developed ACNM showed two characteristic peaks corresponding to the ideal AC samples. The observations from Raman spectra and surface area analysis represent the possibility of extensive SEI formation associated with high surface area. However, the availability of mesopores and micropores in ACNM-2-700 is beneficial in effective lithium storage as well as the formation of stable SEI. Anode half-cells were fabricated using all electrode materials to assess their suitability for LIB applications. A high specific capacity of 610 mAh g⁻¹ at a current rate of 0.1 C was obtained for the ACNM-2-700-based anode. Moreover, the material displayed better stability over 200 cycles for a current rate of 2 C. The rate capability test further validated the efficiency of the anode material for LIBs. SECM scanning of the pristine and cycled anodes validated the effective formation of SEI in a fabricated half-cell. The results of structural and electrochemical characterizations are in agreement. All the reported approach of fabricating electrode material is a straightforward and cost-effective route and thus offers great promise for future energy storage applications.

4. Experimental Section

Materials

The synthesis of AC was carried out with the nutmeg shell waste collected from the local industries of Kerala. Hydrochloric acid (HCl) was purchased from Merck Specialties Private Ltd., India. Sigma-Aldrich Co., USA, supplied polyvinylidene fluoride (PVDF). Lithium hexafluorophosphate (LiPF₆) in a 1:1 (volume/volume ratio) mixture of ethylene carbonate (EC) and dimethyl carbonate (DMC) was obtained from MATLABS, India. Thermo Fisher Scientific India Pvt. Ltd., India, delivered N-methyl pyrrolidone (NMP) and carbon black. Potassium hydroxide (KOH) was provided by Merck Specialties Private Ltd., India. Lithium metal was supplied by Goodfellow Cambridge Ltd., England. All these chemicals were of analytical grade.

Synthesis of ACNMs

In a typical experiment, the chemical activation of nutmeg shell waste, followed by carbonization, was employed for developing ACNM. The detailed procedure was described in our previous works.^[26,34,40] Briefly, to highlight, the KOH-based chemical activation of nutmeg shell waste was done at various activation ratios (wt% of NMS: KOH = 1, 2, and 3). The carbonization of the activated samples was carried out in a tubular furnace at temperatures 500, 600, 700, and 800 °C for 1 h. Continuous Ar (99.99%) supply was provided throughout carbonization. 0.1 M HCl and distilled water were used to maintain the neutral pH of the prepared samples. The as-prepared ACNM samples were dried overnight at 100 °C temperature and labeled as ACNM-1-700, ACNM-2-700, ACNM-3-700, ACNM-2-500, ACNM-2-600, and ACNM-2-800, where (1, 2, 3) represents the activation ratio and (500, 600, 700, and 800 °C) represents carbonization temperature.

Characterizations of ACNMs

The pristine NMS (sample loading ≈5–20 mg) were subjected to TGA analysis using a thermogravimetric analyzer (SDT Q600, TA instruments, USA). TGA was recorded from 30 to 1000 °C under a N₂ atmosphere at a heating rate of 10 °C min⁻¹. The DXR Raman microscope, manufactured by Thermo Scientific, USA, was used for structural studies of ACNMs with a 532 nm laser. Further insights into the AC structure were obtained through XRD analysis (Rigaku Corp., Japan). BET analysis (BELsorp MAX, BEL Japan Inc., Japan) was carried out to understand the pore distribution of ACNMs. Scanning electron microscopy (SEM) was beneficial for understanding the availability of pores in ACNMs. The SEM analysis was done using the EVO18 series, Carl Zeiss Microscopy Ltd., Germany, at 10 kV accelerating voltage. The surface morphology of ACNMs was further analyzed using high-resolution transmission microscopy (HRTEM, FEI, Tecnai G230LaB6 transmission electron microscopy). XPS(PHI Versaprobe III, ULVAC-PHI Inc., USA, equipped with microfocused (200 μm, 15 kV) monochromatic Al-Kα X-ray source ($\hbar\nu = 1486.6$ eV)) was used to explore the surface elemental composition and chemical states of the prepared ACNMs.

Fabrication of Anode Half Cell

A homogeneous slurry with developed ACNM, PVDF, and carbon black was prepared at an 8:1:1 weight ratio. A Cu foil of 40 μm thickness used as a current collector and anodes (mass loading of 2 mg cm⁻²) were developed by tape casting method. An anode and 45 μm-thick lithium disc were sandwiched with the Solupor separator soaked in the LiPF₆ electrolyte. The whole system was inserted in the coin cell of type CR2025. The assembling of half cells was carried out inside a glovebox filled with argon gas. This

meticulous fabrication procedure guarantees that the anode half cells were properly prepared and optimized for the subsequent electrochemical evaluation.

Electrochemical Performance Testing

The half cells were tested over a potential ranging from 0 to 3 V using an SP300 workstation (Biologic Science Instruments, France). CV of the half cell was repeated for five cycles at 0.1 mV s^{-1} scan rate. The GCD analysis was done over a voltage range of 0–3 V. The SEI formation in the AC-based anode material was validated using GCD analysis at different C rates. The rate capability measurement was carried out to study the stability of as-fabricated half cell at 0.1, 1, 2, 3, 4, and 5 C current rates. The cycle stability of ACNM-based anode material was further confirmed by 200 cycles of charging and discharging at 2 C. The SECM470 (Biologic Science Instruments, France) was employed for constant height SDEM measurements of ACNM before and after performing the cycling test. SECM analysis was carried out in a three-electrode configuration. An ultramicroelectrode of diameter $\approx 15 \mu\text{m}$ was used as the working electrode. The reference electrode used was Ag/AgCl; and a platinum rod was employed as a counter electrode, respectively. $\text{Fe}(\text{CN})_6^{3-}/\text{Fe}(\text{CN})_6^{4-}$ was employed as a redox mediator for the analysis. Before the surface scanning, the approach curve was recorded with the microelectrode approaching the ACNM anode at a constant voltage of 0.25 V. The surface scan was carried out for $250 \mu\text{m} \times 250 \mu\text{m}$ at a step size of $5 \mu\text{m}$.

Conflict of Interest

The authors declare no conflict of interest.

Data Availability Statement

The data that support the findings of this study are available from the corresponding author upon reasonable request.

Keywords: anode materials • lithium-ion batteries • pore distributions • scanning electrochemical microscopy • solid-electrolyte interfaces

- [1] Y. Dou, X. Liu, X. Wang, K. Yu, C. Liang, *Mater. Sci. Eng. B* **2021**, *265*, 115015.
- [2] B. Xing, F. Shi, Z. Jin, H. Zeng, X. Qu, G. Huang, C. Zhang, Y. Xu, Z. Chen, J. Lu, *Carbon Energy* **2024**, *6*, e633.
- [3] F. Ahmed, G. Almutairi, P. M. Z. Hasan, S. Rehman, S. Kumar, N. M. Shaalan, A. Aljaafari, A. Alshoaiib, B. AlOtaibi, K. Khan, *Micromachines* **2023**, *14*, 192.
- [4] P. Molaiyan, G. S. Dos Reis, D. Karuppiah, C. M. Subramaniyam, F. García-Alvarado, U. Lassi, *Batteries* **2023**, *9*, 116.
- [5] M. Khan, S. Yan, M. Ali, F. Mahmood, Y. Zheng, X. Song, G. Li, J. Liu, Y. Wang, *Prog. Nat. Sci.: Mater. Int.* **2024**, *34*, 329.
- [6] S. Yaramsetti, M. Girirajan, S. Kalluri, S. Sangaraju, P. S. Maram, *Mater. Chem. Phys.* **2024**, *320*, 129424.
- [7] A. Jain, M. Ghosh, M. Krajewski, S. Kurungot, M. Michalska, *J. Energy Storage* **2021**, *34*, 102178.
- [8] W. Zhao, B. Yan, D. Chen, J. Chen, Q. Zhang, L. Jiang, T. Lan, C. Zhang, W. Yang, S. He, *Colloids Surf., A* **2023**, *668*, 131425.
- [9] A. Hai, G. Bharath, K. R. Babu, H. Taher, M. Naushad, F. Banat, *Process Saf. Environ. Prot.* **2019**, *129*, 103.
- [10] Z. Liu, N. Lin, Y. Wu, J. Li, D. Liu, Y. Wang, H. Lin, *Carbon* **2025**, *231*, 119714.
- [11] Z. Shi, Y. Jin, T. Han, H. Yang, R. Gond, Y. Subasi, H. D. Asfaw, R. Younesi, P. G. Jönsson, W. Yang, *Sci. Rep.* **2024**, *14*, 3966.
- [12] C. Hernández-Renterio, V. Marangon, M. Olivares-Marín, V. Gómez-Serrano, Á. Caballero, J. Morales, J. Hassoun, *J. Colloid Interface Sci.* **2020**, *573*, 396.
- [13] Y. Chu, Y. Shen, F. Guo, X. Zhao, Q. Dong, Q. Zhang, W. Li, H. Chen, Z. Luo, L. Chen, *Electrochem. Energy Rev.* **2020**, *3*, 187.
- [14] N. Nandihalli, *Crystals* **2024**, *14*, 800.
- [15] Y. Astuti, R. R. Insani, A. Z. Ekaningsih, I. Nurhasanah, T. Lestariningsih, A. Suseno, Gunawan, *Results Eng.* **2024**, *24*, 103211.
- [16] Y. Zhang, R. Qiao, Q. Nie, P. Zhao, Y. Li, Y. Hong, S. Chen, C. Li, B. Sun, H. Fan, J. Deng, J. Xie, F. Liu, J. Song, *Nat. Commun.* **2024**, *15*, 4454.
- [17] T. Zhang, J. Mao, X. Liu, M. Xuan, K. Bi, X. L. Zhang, J. Hu, J. Fan, S. Chen, G. Shao, *RSC Adv.* **2017**, *7*, 41504.
- [18] U. Subramanya, C. Chua, V. G. He Leong, R. Robinson, G. A. Cruz Cabiltes, P. Singh, B. Yip, A. Bokare, F. Erogbo, D. Oh, *RSC Adv.* **2019**, *10*, 674.
- [19] T. Thangaselvabai, *Agric. Rev.* **2011**, *32*, 283.
- [20] I. P. S. Kapoor, B. Singh, G. Singh, C. S. De Heluani, M. P. De Lampasona, C. A. N. Catalan, *Int. J. Food Prop.* **2013**, *16*, 1059.
- [21] P. K. Praseetha, E. S. Anooj, *Scopus Ijphrd Citation Score* **2019**, *10*, 1239.
- [22] J. Chen, P. S. Lee, *Adv. Energy Mater.* **2021**, *11*, 2003311.
- [23] W. Li, H. Wang, M. Ouyang, C. Xu, L. Lu, X. Feng, *Energy Convers. Manage.* **2019**, *185*, 211.
- [24] A. Arshansita, L. Jashina, M. Pals, J. Ponomarenko, Y. Akishin, M. Zake, *Energies* **2022**, *15*, 1857.
- [25] H. G. Redda, Y. Nikodimos, W. N. Su, R. S. Chen, S. K. Jiang, L. H. Abrha, T. M. Hagos, H. K. Bezabh, H. H. Weldeyohannes, B. J. Hwang, *Mater. Today Commun.* **2021**, *26*, 102102.
- [26] M. Pulikkottil, H. Antony, M. N. Muralidharan, E. V. Gopalan, S. Ansari, *ChemistrySelect* **2022**, *7*, e202200984.
- [27] S. Ghosh, R. Santhosh, S. Jeniffer, V. Raghavan, G. Jacob, K. Nanaji, P. Kollu, S. K. Jeong, A. N. Grace, *Sci. Rep.* **2019**, *9*, 16315.
- [28] M. V. Kok, E. Ozgur, *Energy Sour. Part A* **2017**, *39*, 134.
- [29] J. R. Garcia, U. Sedran, M. A. A. Zaini, Z. A. Zakaria, *Environ. Sci. Pollut. Res.* **2018**, *25*, 5076.
- [30] I. Nuriskasari, A. Z. Syahrial, T. A. Ivandini, A. Sumboja, B. Priyono, Q. Yan, F. Destyorini, S. Priyono, *Results Eng.* **2024**, *24*, 103273.
- [31] Y. Z. Liang, T. Y. Hsu, Y. S. Su, *ACS Appl. Mater. Interfaces* **2024**, *16*, 29226.
- [32] A. Gajan, C. Lecourt, B. Torres Bautista, L. Fillaud, J. Demeaux, I. T. Lucas, *ACS Energy Lett.* **2021**, *6*, 1757.
- [33] N. Mozhzhukhina, E. Flores, R. Lundström, V. Nyström, P. G. Kitz, K. Edström, E. J. Berg, *J. Phys. Chem. Lett.* **2020**, *11*, 4119.
- [34] P. Merin, P. J. Joy, M. N. Muralidharan, E. V. Gopalan, A. Seema, *Chem. Eng. Technol.* **2021**, *44*, 844.
- [35] S. Yang, K. Zhang, *Nanomaterials* **2018**, *8*, 8040181.
- [36] Q. Feng, J. Jiang, S. Li, G. Zhou, X. Kong, Y. Chen, Q. Zhuang, Z. Ju, *Small* **2025**, *21*, 2406506.
- [37] P. Dubey, V. Shrivastav, M. Singh, P. H. Maheshwari, S. Sundriyal, S. R. Dhakate, *ChemistrySelect* **2021**, *6*, 11736.
- [38] M. Singh, A. Gupta, S. Sundriyal, K. Jain, S. R. Dhakate, *Mater. Chem. Phys.* **2021**, *264*, 124454.
- [39] W. Du, X. Wang, X. Sun, J. Zhan, H. Zhang, X. Zhao, *J. Electroanal. Chem.* **2018**, *827*, 213.
- [40] M. Pulikkottil, A. Thomas, M. Malamal Neelanchery, V. Gopalan Elavumkal, S. Ansari, *Energy Technol.* **2023**, *11*, 2300398.
- [41] T. Ngoc Vo, V. Thuau Le, N. Khoa Dang, M. Loan Phung Le, V. Hoang Nguyen, V. Man Tran, M. Thu Nguyen, N. Hoa Thi Tran, T. Loi Nguyen, I. Tae Kim, H. Chi Minh City, L. Trung Ward, T. Duc District, *Biomass Bioenergy* **2024**, *181*, 107058.
- [42] T. Sesuk, P. Tammarat, P. Jivaganont, K. Somton, P. Limthongkul, W. Kobsiriphat, *J. Energy Storage* **2019**, *25*, 100910.
- [43] B. Aktekin, L. M. Rieger, S. K. Otto, T. Fuchs, A. Henss, J. Janek, *Nat. Commun.* **2023**, *14*, 6946.
- [44] Y. Liu, H. Zhang, X. Li, L. Wang, Y. Dong, W. Li, J. Zhang, *Appl. Catal., A* **2021**, *611*, 117902.
- [45] M. Rajesh, R. Manikandan, S. Park, B. C. Kim, W. J. Cho, K. H. Yu, C. J. Raj, *Int. J. Energy Res.* **2020**, *44*, 8591.
- [46] D. C. Martínez-Casillas, I. Mascorro-Gutiérrez, C. E. Arreola-Ramos, H. I. Villafán-Vidales, C. A. Arancibia-Bulnes, V. H. Ramos-Sánchez, A. K. Cuentas-Gallegos, *Carbon N Y* **2019**, *148*, 403.
- [47] B. Deng, Q. Huang, W. Zhang, J. Liu, Q. Meng, Z. Zhu, W. Zhong, X. Li, Y. Zhang, *J. Cleaner Prod.* **2021**, *309*, 127391.
- [48] C. Senthil, J. W. Park, N. Shaji, G. S. Sim, C. W. Lee, *J. Energy Chem.* **2021**, *64*, 286.
- [49] P. U. Nzereogu, A. D. Omah, F. I. Ezema, E. I. Iwuoha, A. C. Nwanya, *Appl. Surf. Sci. Adv.* **2022**, *9*, 100233.
- [50] T. Kim, W. Choi, H. C. Shin, J. Y. Choi, J. M. Kim, M. S. Park, W. S. Yoon, *J. Electrochem. Sci. Technol.* **2020**, *11*, 14.
- [51] W. Yu, K. Y. Lin, D. T. Boyle, M. T. Tang, Y. Cui, Y. Chen, Z. Yu, R. Xu, Y. Lin, G. Feng, Z. Huang, *Nat. Chem.* **2025**, *17*, 246.

- [52] H. Lu, M. Nagarathinam, Y. Chen, W. Zhang, X. Chen, J. Chen, J. Tao, J. Li, Y. Lin, O. Kolosov, Z. Huang, *Small Methods* **2025**, 2401786.
- [53] C. Hernández-Rentero, V. Marangon, M. Olivares-Marín, V. Gómez-Serrano, Á. Caballero, J. Morales, J. Hassoun, *J. Colloid Interface Sci.* **2020**, 573, 396.
- [54] K. Ge, Z. Wang, J. Liu, Y. Mu, R. Wang, X. Xu, Y. Wang, Z. Zou, Q. Zhang, M. Han, L. Zeng, *Adv. Funct. Mater.* **2025**, 35, 2414384.
- [55] S. Y. Lee, Y. Choi, J. K. Kim, S. J. Lee, J. S. Bae, E. D. Jeong, *J. Indust. Eng. Chem.* **2021**, 94, 272.
- [56] T. T. Mai, D. L. Vu, D. C. Huynh, N. L. Wu, A. T. Le, *J. Sci. Adv. Mater. Dev.* **2019**, 4, 223.
- [57] S. Wu, Y. Zhang, H. Liang, H. Pan, L. Chen, Y. Jiang, H. Ding, P. Wang, D. Zhao, Q. Zhang, L. Zeng, *Energy Storage Mater.* **2025**, 75, 104024.
- [58] L. Xie, C. Tang, Z. Bi, M. Song, Y. Fan, C. Yan, X. Li, F. Su, Q. Zhang, C. Chen, *Adv. Energy Mater.* **2021**, 11, 01650.
- [59] Z. Li, S. Li, T. Wang, K. Yang, Y. Zhou, Z. Tian, *J. Electrochem. Soc.* **2021**, 168, 090513.
- [60] F. Xie, S. Zhao, X. Bo, G. Li, J. Fei, E. A. M. A. Ahmed, Q. Zhang, H. Jin, S. Wang, Z. Lin, *J. Mater. Chem. A* **2022**, 11, 53.
- [61] M. Piglowska, B. Kurc, Ł. Rymaniak, *Waste Biomass Valoriz.* **2023**, 14, 2401.
- [62] L. E. Strange, X. Li, E. Wornyo, M. Ashaduzzaman, S. Pan, *Chem. Biomed. Imaging* **2023**, 1, 110.
- [63] J. Yan, J. Yao, J. Zhao, Z. Yu, Z. Ye, L. Zhang, Z. Wang, X. Zhang, Z. Rong, D. Kong, J. Sun, *Adv. Funct. Mater.* **2025**, 2421918.
- [64] A. G. Elang Barruna, R. Muhamad Naufal, M. R. Nugraha, I. Subiyanto, N. Tinapilla, A. Subhan, H. Chairul, *IOP Conf. Ser.: Earth Environ. Sci.* **2021**, 673, 012018.
- [65] K. Yu, J. Li, H. Qi, C. Liang, *Diamond Relat. Mater.* **2018**, 86, 139.
- [66] S. Zheng, J. Zhang, H. Deng, Y. Du, X. Shi, *J. Bioresour. Bioproducts* **2021**, 6, 142.
- [67] A. V. Baskar, G. Singh, A. M. Ruban, J. M. Davidraj, R. Bahadur, P. Sooriyakumar, P. Kumar, A. Karakoti, J. Yi, A. Vinu, *Adv. Funct. Mater.* **2023**, 33, 08349.

Manuscript received: March 25, 2025

Revised manuscript received: May 28, 2025

Version of record online: